Chinese Journal of
POLYMER SCIENCE

RESEARCH ARTICLE

https://doi.org/10.1007/s10118-026-3660-3
Chinese J. Polym. Sci. **2026**, *44*, 2524–2533

Boosting Blood-Brain Barrier Crossing with a Mannosylated Nanocarrier

Nan-Nan Gu[a], Ping Wei[a*], Jin-Hui Jiang[b*], and Jing-Hua Chen[a*]

[a] *School of Life Sciences and Health Engineering, Jiangnan University, Wuxi 214122, China*
[b] *Department of Polymeric Materials, School of Materials Science and Engineering, Tongji University, Shanghai 201804, China*

Electronic Supplementary Information

Abstract The blood-brain barrier (BBB) is a major obstacle to the delivery of most therapeutic molecules to the brain, thereby preventing the effective treatment of numerous neurological disorders. However, this barrier can be bypassed by exploiting receptors and transport proteins that are highly expressed in the brain capillary endothelial cells (BCECs). Given the overexpression of glucose transporter 1 (GLUT1) at the BBB and in glioma cells, a mannosylated nanocarrier was developed as a potential dual-targeted drug delivery system to enhance BBB penetration *via* GLUT1-mediated transcytosis and improve drug accumulation in glioma cells *via* GLUT1-mediated endocytosis. *In vitro* physicochemical characterization revealed that the mannosylated nanocarrier presented a satisfactory size of 123 nm with a uniform distribution and high encapsulation efficiency for a newly developed aggregation-induced emission (AIE) photosensitizer. Our findings revealed that this mannosylated nanocarrier represents a promising nanoplatform capable of crossing the BBB and enabling effective photodynamic therapy.

Keywords Self-assembly; Blood-brain barrier; Photodynamic therapy; Aggregation-induced emission

Citation: Gu, N. N.; Wei, P.; Jiang, J. H.; Chen, J. H. Boosting blood-brain barrier crossing with a mannosylated nanocarrier. *Chinese J. Polym. Sci.* **2026**, *44*, 2524–2533.

INTRODUCTION

The blood-brain barrier (BBB) is the most sophisticated protective structure of the central nervous system and poses a significant challenge in modern neuropharmaceutical development.[1,2] Functioning as a dynamic interface,[3,4] the BBB is primarily composed of tightly connected brain microvascular endothelial cells, a highly specialized basement membrane, embedded pericytes, astrocytes, and microglia.[5,6] This complex cellular ensemble forms a highly selective semi-permeable membrane that regulates the exchange of substances with the bloodstream, according to the physiological needs of the brain.[7,8,9] Consequently, the BBB prevents the effective entry of most therapeutics for central nervous system (CNS) diseases.[10,11] Therefore, enhancing drug permeability across the BBB has become a critical research direction for neurotherapeutics.[12,13]

Efficient delivery of therapeutics to brain lesions requires overcoming formidable obstacles presented by the BBB. Drug delivery across the BBB occurs mainly *via* passive paracellular diffusion and active transcellular transport mechanisms, such as receptor-, carrier-, adsorption-, and cell-mediated transport.[14,15] Among these, the carrier-mediated transport strategy is particularly attractive because of its ability to harness endogenous physiological pathways, thus providing high transport efficiency, inherent brain specificity, and preservation of BBB integrity. Research indicates that Glucose transporter 1 (GLUT1) is highly and constitutively expressed in the brain capillary endothelial cells. Under specific physiological conditions, such as a rapid blood glucose increase, GLUT1 translocates from the luminal to the abluminal plasma membrane.[16,17] This phenomenon provides an opportunity to utilize natural substrates such as mannose to mediate drug delivery.[18,19] Surface modification of nanocarriers with mannose is a promising strategy for significantly enhancing BBB penetration and subsequent brain accumulation *via* this physiological route.

In this study, we designed an amphiphilic copolymer modified with mannose that can self-assemble into well-defined nanoparticles. Photodynamic therapy (PDT) is a minimally invasive treatment strategy that has considerable potential.[20,21,22,23] Therefore, we loaded a novel type-I photosensitizer into the nanoparticles. Unlike previously reported photosensitizers, the photosensitizer in this work offers a dual advantage: first, it can simultaneously generate two types of type-I radicals to more effectively counteract the hypoxic tu-

* Corresponding authors, E-mail: weiping@jiangnan.edu.cn (P.W.)
E-mail: Jinhui_JIANG@alumni.tongji.edu.cn (J.H.J.)
E-mail: chenjinghua@jiangnan.edu.cn (J.H.C.)
Received January 22, 2026; Accepted March 11, 2026; Published online May 30, 2026

mor microenvironment; second, it possesses a pronounced aggregation-induced emission (AIE) effect, where its fluorescence is greatly enhanced in the aggregated state within the nanoparticles, enabling potential visualization and monitoring of the treatment process.[24,25,26,27,28] The prepared nanocarrier system exhibited characteristics such as small size, high stability, and a negatively charged surface. *In vitro* experiments confirmed that this system effectively generated reactive oxygen species (ROS) and demonstrated potent PDT effects in C6 glioma cells. To evaluate BBB-crossing capability, this study innovatively established physiologically relevant *in vitro* BBB models. Beyond the conventional monolayer transwell model, a three-dimensional (3D) multicellular spheroid model was developed to better simulate the tight intercellular connections and spatial heterogeneity found *in vivo*,[29,30] thereby providing a more reliable predictive platform for assessing the barrier-penetrating efficacy of nanomedicines. Ultimately, this study aims to leverage the mannose-mediated GLUT1 transport pathway to achieve efficient BBB traversal and targeted accumulation of nanocarriers in brain lesions (Scheme 1), offering a novel strategy for the precise diagnosis and treatment of brain disease.

EXPERIMENTAL

The experimental sections are available in the electronic supplementary information (ESI).

RESULTS AND DISCUSSION

Preparation and Characterization of MAN-DSPE-PEG$_{2000}$ NPs

The photophysical characteristics of TQBrOH were characterized by UV-Vis and photoluminescence (PL) spectroscopy. Building on the AIE property of TQBrOH, which exhibits significantly stronger luminescence in the aggregated state compared to the conventional aggregation-caused quenching effect,[31] we encapsulated TQBrOH into nanoparticles for UV-Vis and fluorescence spectroscopic analyses. As shown in Fig. 1(a), the tests indicated that TQBrOH@NPs exhibited an excitation wavelength of 500 nm and an emission wavelength of 660 nm, indicating their potential for bioimaging applications.[32,33]

To make the TQBrOH molecule water soluble and subsequently stable in the bloodstream, we employed amphiphilic copolymers with excellent biocompatibility, namely DSPE-PEG$_{2000}$ and MAN-DSPE-PEG$_{2000}$, and prepared hydrophilic negatively charged nanoparticles. As shown in Fig. 1(c), the average hydrodynamic diameters of DSPE-PEG$_{2000}$ nanoparticles (DP NPs) and mannose-modified DSPE-PEG$_{2000}$ nanoparticles (MAN-DP NPs) in aqueous suspension were 125 and 123 nm, respectively, with a narrow size distribution (polydispersity index (PD) = 0.192 and 0.204, respectively). Upon loading with TQBrOH, the average hydrodynamic diameters of the resulting TQBrOH@DP and TQBrOH@MAN-DP NPs decreased slightly to 105 nm and 101 nm, respectively (Fig. 1d). The decrease in nanoparticle size after TQBrOH loading is speculated to be due to the strong hydrophobic interaction between the hydrophobic structure of TQBrOH and the fatty chain of the DSPE. This interaction promotes a tighter and more ordered arrangement of the molecules in the hydrophobic core. Additionally, the zeta potential of the nanoparticles increased from –16.5 and –13.9 mV to –11.5 and –11.2 mV after the incorporation of TQBrOH (Fig. 1b). The increase in the zeta potential was attributed to the small positive charge carried by TQBrOH.

Transmission electron microscopy (TEM) was used to inves-

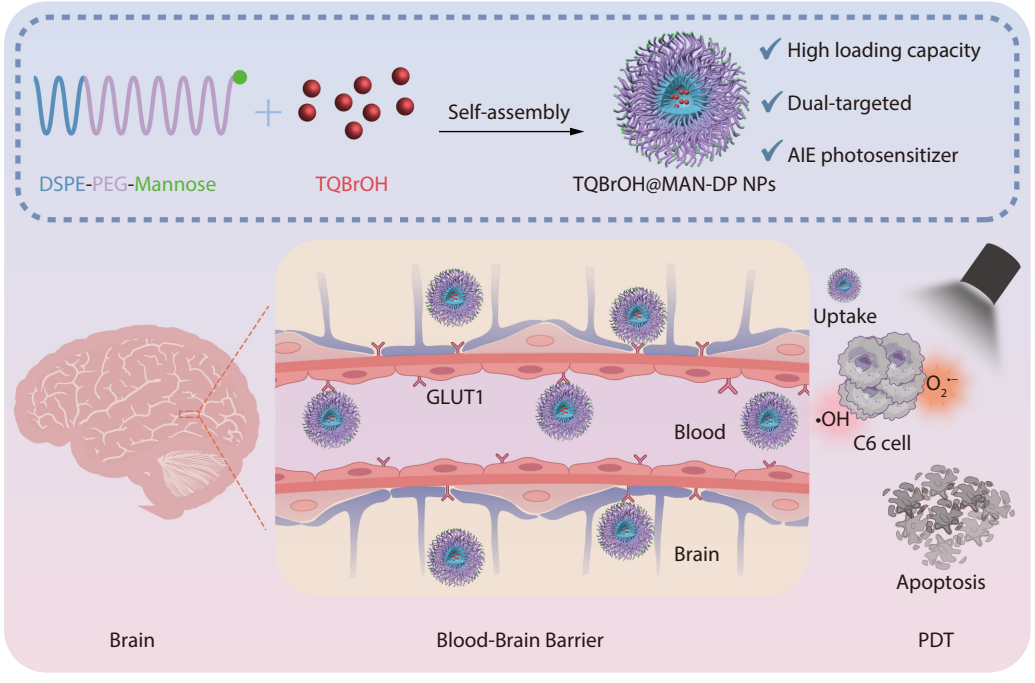

Scheme 1 Schematic illustration of the self-assembled nanoparticles crossing the blood-brain barrier and exerting potent photodynamic therapy effects.

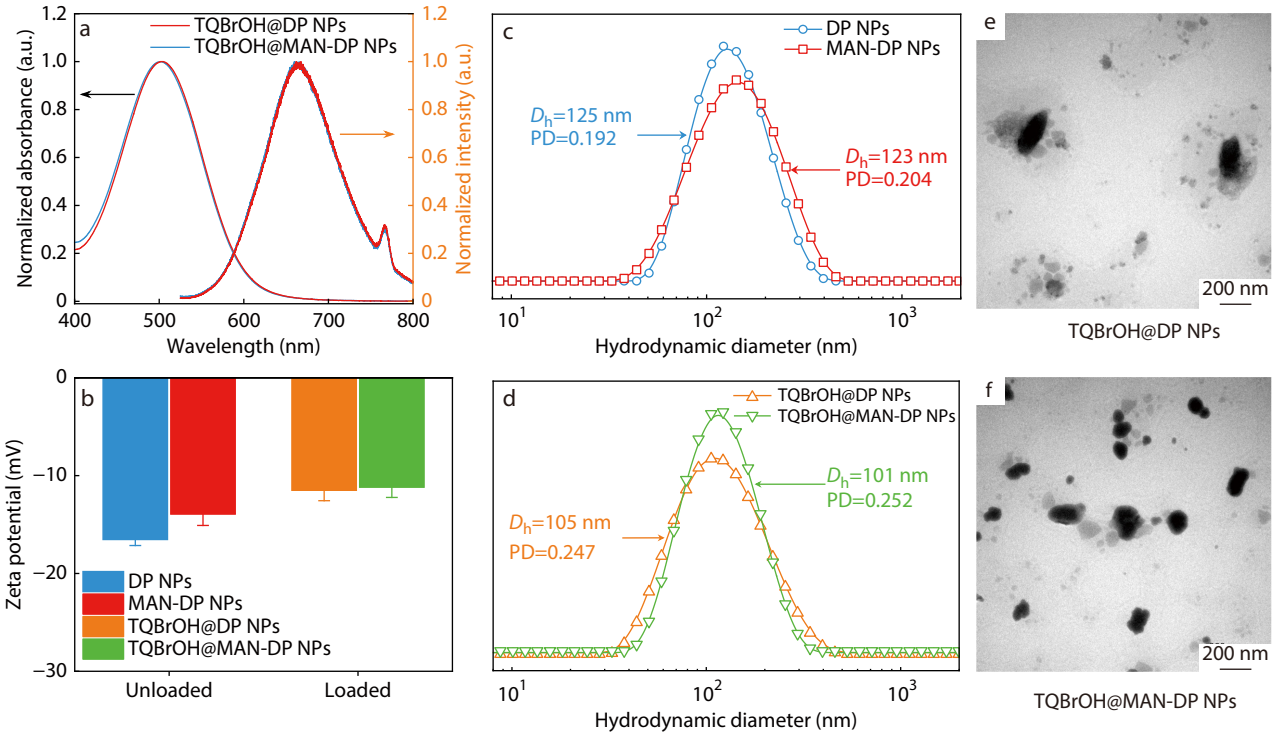

Fig. 1 (a) Normalized absorption and fluorescence spectra of TQBrOH@DP NPs and TQBrOH@MAN-DP NPs in aqueous solution (30 μmol/L for TQBrOH); (b) Zeta potential of unloaded and TQBrOH-loaded nanoparticles. (c) and (d) Size distribution of unloaded and TQBrOH-loaded nanoparticles as determined by DLS study. TEM images of (e) TQBrOH@DP NPs and (f) TQBrOH@MAN-DP NPs.

tigate the morphology of the nanoparticles. The images in Figs. 1(e) and 1(f) confirm the classic micellar structure of the nanoparticles after TQBrOH loading. Both TQBrOH@DP and TQBrOH@MAN-DP NPs exhibited good dispersibility without significant agglomeration. From a morphological perspective, mannose modification did not cause significant changes in the basic structure of the nanoparticles, and TQBrOH@DP NPs and TQBrOH@MAN-DP NPs showed consistency in size and morphology, consistent with previous results of similar particle sizes measured by dynamic light scattering (DLS).

Detection of Extracellular ROS Generation

To investigate the types of ROS produced by TQBrOH, we used different ROS indicators to detect the production of different ROS. First, we used the classical ROS indicator, dichlorofluorescein (DCFH-DA), for the total ROS generated by TQBrOH. The green fluorescence of DCFH can be excited by any type of ROS; therefore, its fluorescence intensity represents the total amount of ROS produced in the system. As shown in Fig. 2(a), strong DCF fluorescence was observed for both TQBrOH@DP and TQBrOH@MAN-DP NPs, with comparable emission intensities. This indicates that TQBrOH generated similar levels of ROS in both nanoparticles and that the nanoparticles had a negligible impact on the ROS production of TQBrOH.

As the key element of PDT, photosensitizers are categorized by their mechanism into Type I (electron/proton transfer) and Type II (energy transfer) agents. Multiple ROS indicators were employed to accurately identify the type of ROS produced by loaded TQBrOH. Following the initial screening of total ROS levels using the conventional probe DCFH-DA, multiple highly specific ROS indicators were utilized for systematic validation. First, 9,10-anthracene-bis(methylene) dimeric acid (ABDA) was used to detect the generation of singlet oxygen ($^1O_2$) in the system. As shown in Fig. 2(b), there was nearly no significant change in the TQBrOH@DP NPs and TQBrOH@MAN-DP NPs before and after white light irradiation, indicating that TQBrOH is a Type I photosensitizer. The reaction mechanism of type I photosensitizers is independent of oxygen, enabling effective functionality even within the hypoxic microenvironment commonly found in tumor tissues. This characteristic represents a significant advantage over the type II photosensitizers.[34,35]

Superoxide anions ($O_2^{\bullet-}$) and hydroxyl radicals (•OH) in the system were detected using dihydrorhodamine 123 (DHR123) and hydroxyphenyl fluorescein (HPF), respectively. Figs. 2(c) and 2(d) show that TQBrOH generates both $O_2^{\bullet-}$ and •OH, as indicated by the enhanced DHR123 and HPF fluorescence, respectively. Notably, while $O_2^{\bullet-}$ production is oxygen-dependent, the effective generation of •OH suggests a complementary mechanism that remains active under hypoxic conditions.

To investigate the effects of the photodynamic parameters on ROS generation, we systematically evaluated the effects of light dose, irradiation time, and nanoparticle concentration (Fig. S7 in ESI). The results showed that ROS production increased with higher nanoparticle concentrations and longer irradiation times. However, a slight decrease was observed when the light intensity was too high, which may be due to photobleaching. Based on these findings, a lower light intensity combined with a longer irradiation time was selected for subsequent experiments to ensure a sufficient light dose while minimizing photobleaching risk. Although this *in vitro*

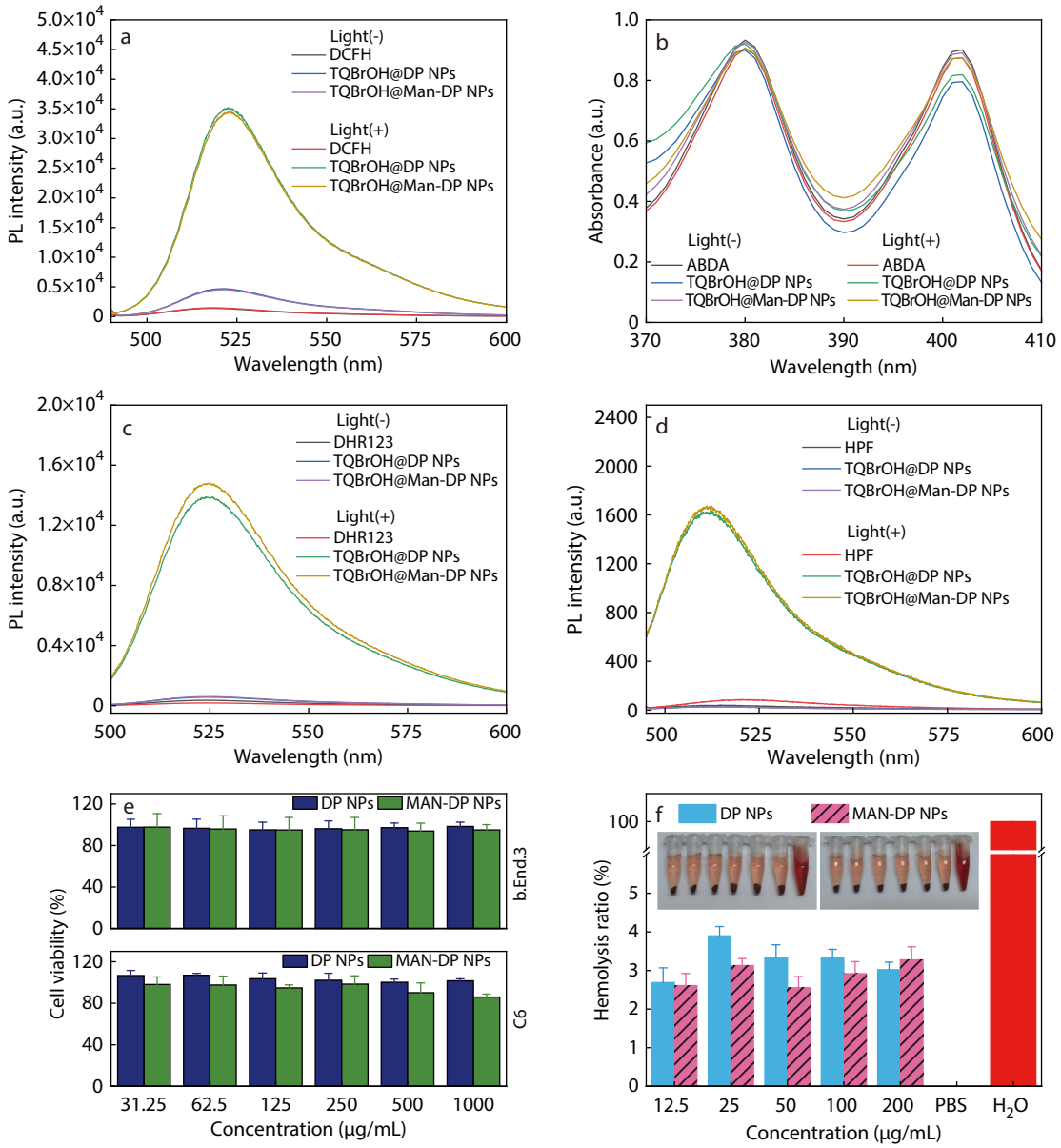

Fig. 2 (a) PL spectra of DCFH in water and in the present of nanoparticles after exposure to white light irradiation; (b) Absorption spectra of ABDA in water and in the presence of a nanoparticles after exposure to white light irradiation; (c) PL spectra of DHR123 in water and in the presence of a nanoparticles after exposure to white light irradiation; (d) PL spectra of HPF in water and in the presence of a nanoparticles after exposure to white light irradiation; (e) Cytotoxicity of different concentrations of nanoparticles on C6 and b.End.3 cells (n=5); (f) Hemolysis rate of nanoparticles at different concentrations (n=3).

optimization provides a foundation for parameter selection, clinical application necessitates further *in vivo* studies accounting for tissue light penetration and tumor physiology.

Cytotoxicity and Hemolytic Assay

An ideal drug delivery carrier first needs to have good cell and blood compatibility. To this end, we first evaluated the cytotoxicity of DP NPs and MAN-DP NPs in b.End.3 cells and C6 cells. As shown in Fig. 2(e), the relative cell viability remained above 85% in the different concentration treatment groups, indicating no significant cytotoxicity within the tested concentration range, with the highest concentration reaching 1.0 mg/mL. In addition, we conducted hemolysis experiments to evaluate the blood compatibility of DP and MAN-DP NPs. As shown in Fig. 2(f), within the tested concentration range, all hemolysis rates were below 4%, indicating that DP and MAN-DP NPs did not cause significant hemolysis.[36,37]

Cellular Uptake

Beyond its high ROS generation efficiency, TQBrOH exhibits a fluorescence emission maximum at 660 nm, endowing it with favorable imaging properties. This integrated functionality allows its cellular uptake to be tracked directly by flow cytometry and its distribution to be visualized by CLSM, eliminating the need for additional fluorescent dyes. As shown in Figs. 3(a) and 3(b), after incubation for 4 h, the uptake rates of TQBrOH@DP

NPs and TQBrOH@MAN-DP NPs by b.End.3 cells and C6 cells reached almost 99%. The experimental results revealed that under the present conditions, cells possessed a remarkably high basal endocytic capacity for DP NPs, effectively saturating the measurable uptake range. Even if specific mannose-mediated endocytosis exists, the uptake rate cannot reflect such differences.

GLUT1-dependent Uptake of MAN-DP NPs

The GLUT1 inhibition assay using WZB117[38,39] provided direct evidence for the involvement of GLUT1 in the cellular uptake of MAN-DP NPs. As shown in Figs. 3(c) and 3(d), MAN-DP NPs exhibited significantly higher cellular uptake compared to DP NPs without WZB117 and showed significantly higher mean fluorescence intensity (MFI) than DP NPs (p<0.001). To assess the role of GLUT1 in this enhanced uptake, cells were pretreated with the GLUT1 inhibitor WZB117. As shown in Figs. 3(c) and 3(d), WZB117 treatment markedly reduced the MFI of MAN-DP NPs in b.End.3 cells (p<0.001) but had no significant effect on DP NPs. These results conclusively demonstrated that GLUT1 mediates the enhanced uptake of MAN-DP NPs, supporting the proposed mechanism of GLUT1-targeted delivery for BBB penetration and glioma cell recognition.

Intracellular Localization

Confocal microscopy results shown in Figs. 3(e) and 3(f) that TQBrOH@DP NPs and TQBrOH@MAN-DP NPs were distributed in the cytoplasm and did not enter the nucleus, whether in b.End.3 cells or C6 cells. The widespread cytoplasmic localization of nanoparticles ensures that the generated ROS can act on a larger intracellular area and affect multiple critical organelles (*e.g.*, mitochondria and endoplasmic reticulum), thereby maximizing the therapeutic outcome of photodynamic therapy.

Detection of Intracellular ROS Generation

Intracellular ROS generation induced by TQBrOH was assessed using a DCFH-DA fluorescent probe. The fluorescence images in Fig. 4 show obvious green fluorescence intensity in both the TQBrOH@DP NPs and TQBrOH@MAN-DP NPs groups, demon-

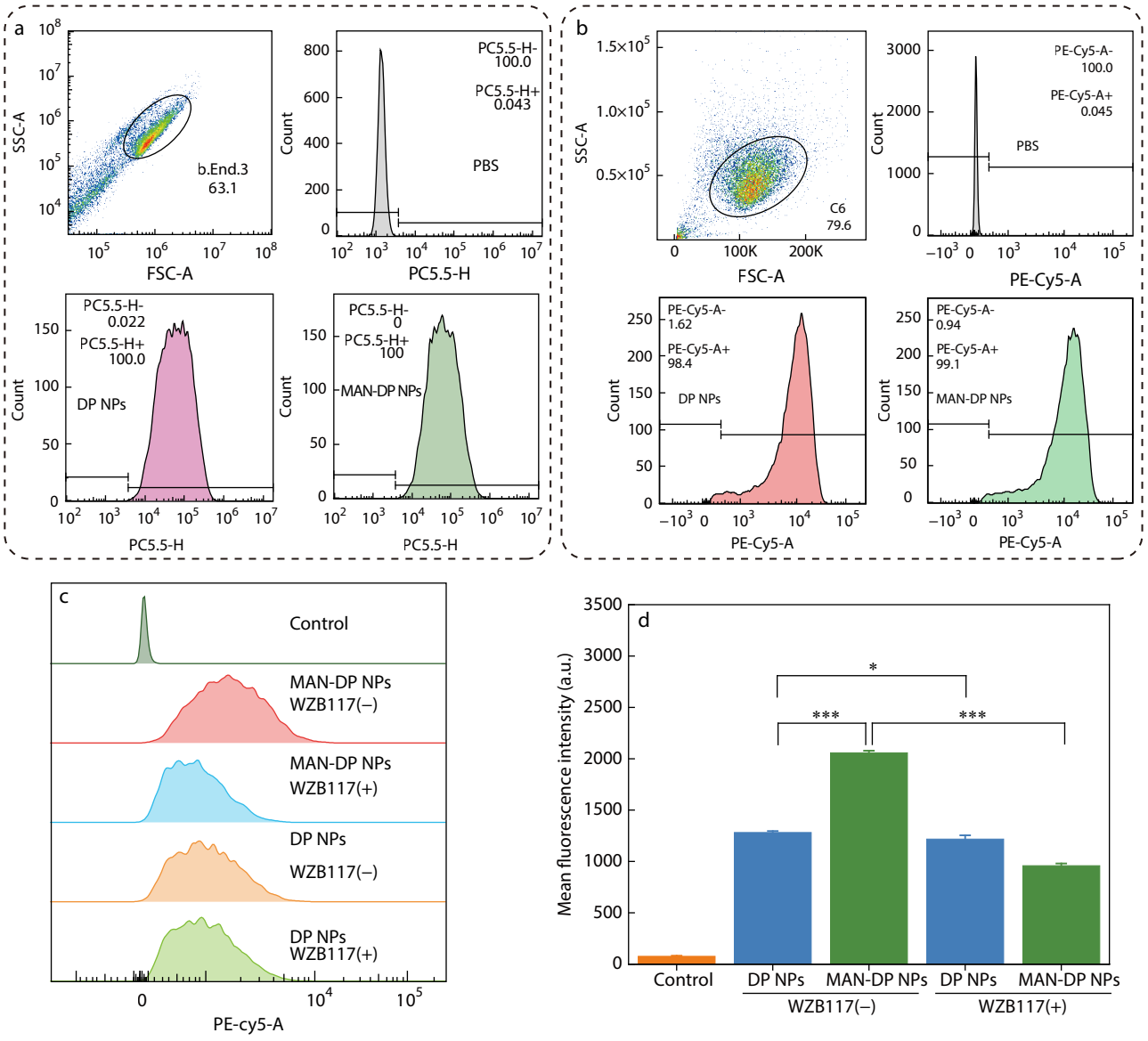

https://doi.org/10.1007/s10118-026-3660-3

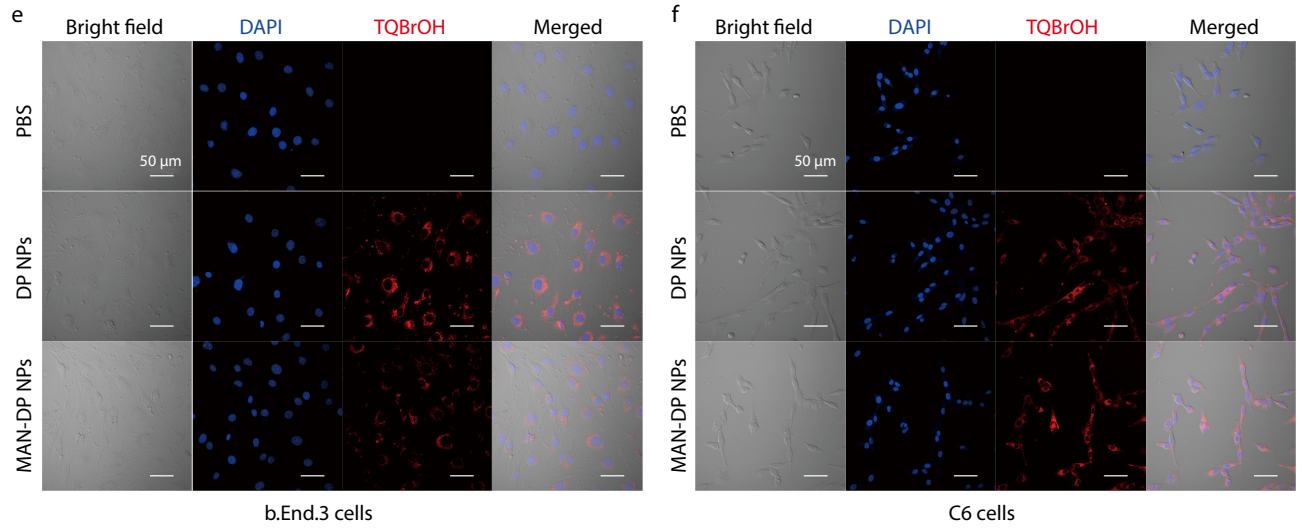

Fig. 3 (a, b) Flow cytometry detection of b.End.3 and C6 cell uptake of TQBrOH@DP NPs and TQBrOH@MAN-DP NPs. Both the PC5.5 and PE-Cy5 channels were used to detect the red fluorescence derived from TQBrOH. (c) TQBrOH fluorescence intensity distribution in b.End.3 across treatment groups. n=3. (d) Mean fluorescence intensity (MFI) of TQBrOH in b.End.3 cells as determined by flow cytometry. Data are presented as mean ± standard deviation (n=3). Statistical analysis was performed using ANOVA analysis (*) for $p < 0.05$, (**) for $p < 0.01$, (***) for $p < 0.001$, n=3. (e, f) Confocal microscopy imaging of the intracellular localization of nanoparticles in b.End.3 and C6 cells. Blue channel: DAPI-stained nuclei. Red channel: TQBrOH-labelled nanoparticles. Scale bar: 50 μm.

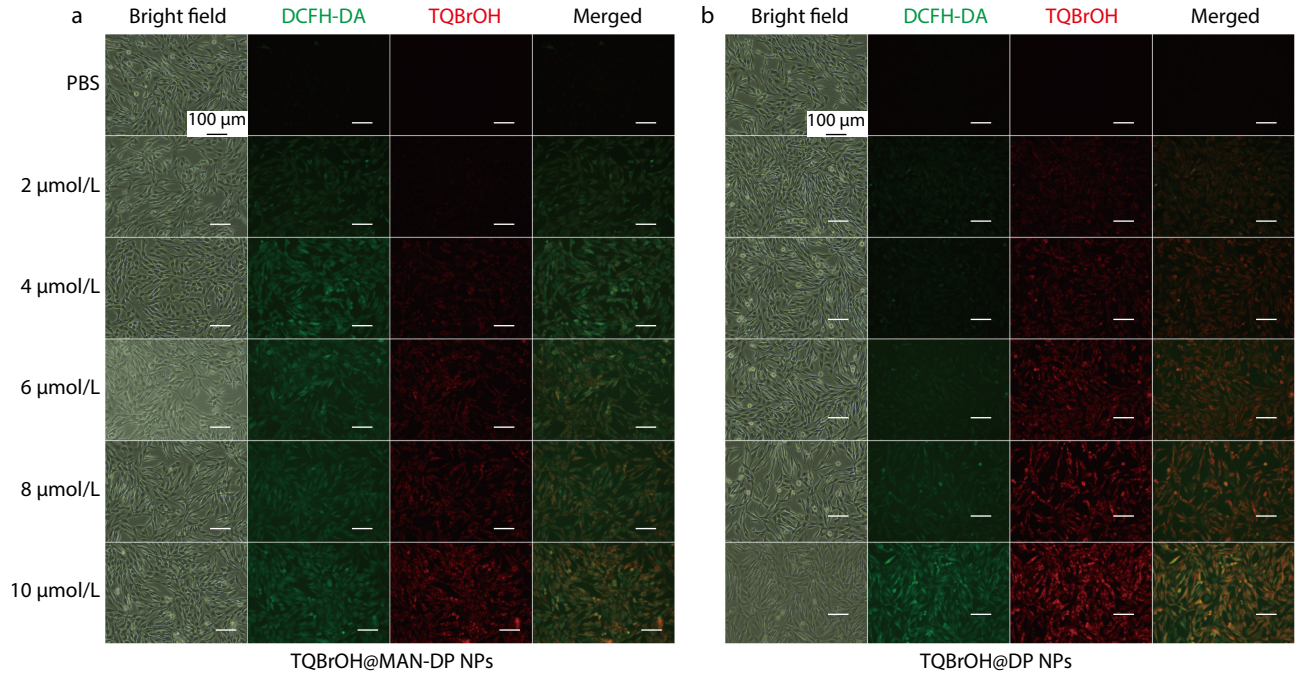

Fig. 4 Detection of intracellular ROS levels with (a) TQBrOH@MAN-DP NPs and (b) TQBrOH@DP NPs. Scale bar: 100 μm.

strating plenty of intracellular ROS generation. Moreover, the amount of ROS generated within cells was positively correlated with the concentration of TQBrOH.

Evaluation of Permeability in the Biomimetic BBB Models

To verify whether mannose-modified nanoparticles can penetrate the BBB, we constructed an BBB model *in vitro*. As shown in Fig. 5(a), b.End.3 cells were seeded on the upper layer to simulate endothelial cells, and C6 tumor cells were seeded on the lower layer. By adding TQBrOH@DP and TQBrOH@MAN-DP NPs at the same concentration to the upper layer and collecting the lower layer cells at different times, the uptake of cells was confirmed by flow cytometry. As shown in Fig. 5(b), after 4 h of uptake by the lower C6 cells, the uptake rate of DP NPs reached 63.2%, whereas that of MAN-DP NPs reached 65.1%. However, after 8 h of uptake, both the uptake rates reached 99%. Although lower-chamber cellular uptake serves as an indirect measure of permeability, this observation can likely be attributed to the transwell monolayer model, which simulates a static,

https://doi.org/10.1007/s10118-026-3660-3

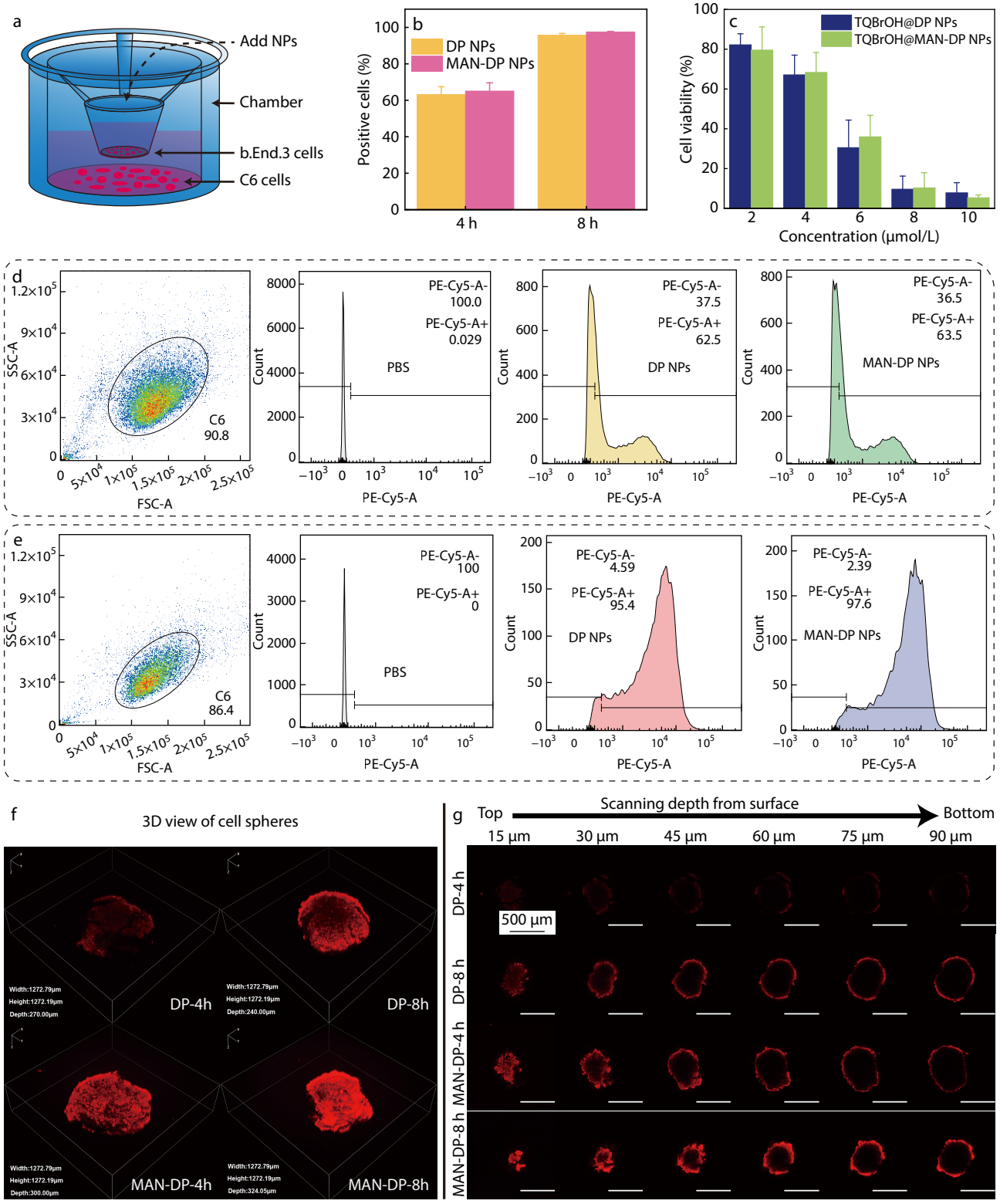

Fig. 5 (a) Schematic representation of the construction process *in vitro* for BBB; (b) Uptake rate of C6 cells in the lower layer at 4 h and 8 h in Transwell experiment; (c) The therapeutic effect of PDT on C6 cells (n=3); (d) and (e) Flow cytometry of C6 cells in the lower layer at 4 h and 8 h in Transwell experiment; (f) Full view of 3D cell sphere uptake of nanoparticles at 4 h and 8 h; (g) Z-axis slice scanning images of 3D cell spheres uptake of nanoparticles at 4 h and 8 h. Scale bar: 500 μm.

fully confluent vascular endothelial barrier. Under such conditions, the transcellular transport of TQBrOH@DP and TQBrOH@MAN-DP NPs was governed predominantly by passive diffusion mechanisms. Although an active uptake pathway

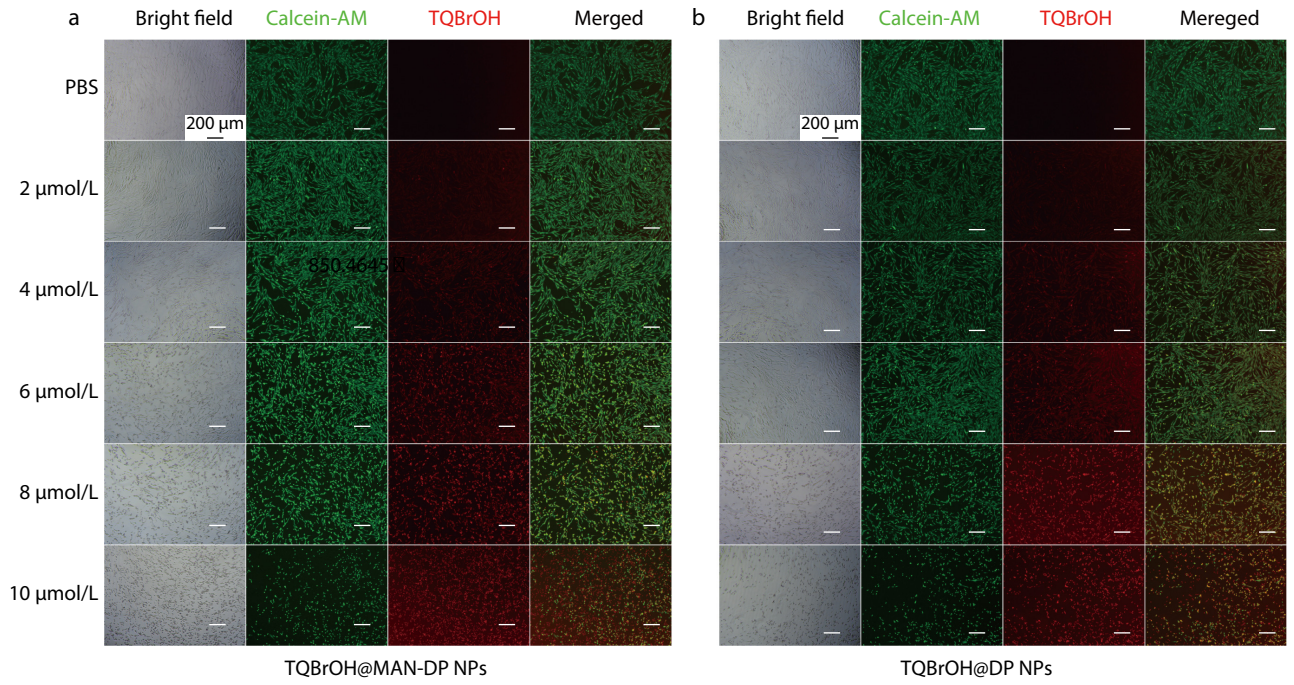

Fig. 6 Representative fluorescence images of C6 cells stained with calcein-AM after treated with (a) TQBrOH@MAN-DP NPs, and (b) TQBrOH@DP NPs. Scale bar: 200 μm.

mediated by mannose may exist, its contribution to the total flux is not significant compared to efficient passive diffusion; thus, failing to demonstrate any modification advantage. The specific results of flow cytometry are shown in Figs. 5(d) and 5(e), indicating that the uptake rates of TQBrOH@DP NPs and TQBrOH@MAN-DP NPs were comparable at 4 and 8 h. Although our BBB model validation provides reasonable evidence of barrier integrity, additional validation steps for comprehensive barrier characterization remain to be performed in future studies.

Therefore, following the initial evaluation of nanoparticle permeability using a transwell monolayer assay, we developed a three-dimensional multicellular spheroid model to assess penetration under more physiologically relevant and structurally complex conditions. After the formation of the cell spheres, we measured the uptake rate of cells at 4 and 8 h. The difference is that we used confocal 3D scanning technology to capture cell spheres and determine the uptake rate and depth of cells based on the fluorescence intensity. As shown in the Figs. 5(f) and 5(g), after 4 and 8 h of uptake, it can be clearly seen that the fluorescence intensity of the MAN-DP NPs group is higher and the uptake depth is deeper. The superior penetration of MAN-DP NPs into the complex 3D co-culture model can be attributed to a fundamental shift in their transport mechanisms. Specifically, mannose ligands transform the particle behavior from reliance on passive diffusion to active receptor-mediated cross-cellular transport.

As shown in Fig. S9(a) (in ESI), MAN-DP NPs exhibited substantially higher mean fluorescence intensity than DP-NPs throughout the entire cell spheroid at both 4 h and 8 h time points. The radial fluorescence intensity profile was measured at the maximal cross-section (equatorial plane) of the spheroids. As shown in Fig. S9(b) (in ESI), MAN-DP NPs exhibited superior fluorescence intensity as well as deeper penetration at the 8 h time point. This suggests thatMAN-DP NPs demonstrated superior penetration capability compared to DP-NPs.

In vitro Phototherapeutic Study

The aggressive nature, poor prognosis, and high mortality of CNS tumors, such as gliomas, make their treatment exceptionally challenging.[40,41,42] Accordingly, C6 cells were chosen as the PDT targets. To investigate the killing effect of TQBrOH on C6 tumor cells, we used the CCK-8 assay and live/dead staining. Under certain irradiation conditions, the higher the concentration of TQBrOH, the higher is the cell mortality rate. As shown in Fig. 5(c), at a concentration of 10 μmol/L, after PDT, cell viability decreased to below 10%. Live/dead staining using only calcein-AM (which labels live cells) demonstrated a progressive loss of viable cells with increasing TQBrOH concentrations, accompanied by distinct morphological changes. These observations were consistent with the concentration-dependent photodynamic killing effect of TQBrOH (Figs. 6a and 6b).

CONCLUSIONS

In summary, this study successfully constructed a potential dual-targeted drug delivery system that enhances BBB penetration by utilizing GLUT-mediated transcellular transport. In response to the insufficient efficiency of traditional nanoparticle brain targeting, this study adopted a surface engineering strategy to enhance the affinity of nanoparticles with GLUT1 on the BBB through mannosylation, overcoming the limitations of passive targeting strategies relying solely on size effects. The experimental results demonstrated that this system exhibits excellent penetration ability in a three-dimensional biomimetic BBB model, effectively overcoming the predictive limitations of tradition-

al two-dimensional models through the synergy of active targeting and physiologically relevant validation. In addition, the encapsulated TQBrOH photosensitizer was found to generate highly efficient generation of type I radicals upon irradiation, exhibiting excellent photodynamic therapeutic efficacy. Although the above results are highly promising, these findings require validation in further *in vivo* studies using orthotopic glioma models. Overall, this study provides a conceptual validation for brain-targeted PDT and has important theoretical and clinical significance for promoting the development of targeted therapy strategies for central nervous system diseases.

Conflict of Interests

The authors declare no interest conflict.

Electronic Supplementary Information

Electronic supplementary information (ESI) is available free of charge in the online version of this article at http://doi.org/10.1007/s10118-026-3660-3.

Data Availability Statement

The data that support the findings of this study are available upon request from the corresponding authors.

ACKNOWLEDGMENTS

This study was financially supported by the National Natural Science Foundation of China (No. 22305102).

REFERENCES

1 Zhao, Z.; Nelson, A. R.; Betsholtz, C.; Zlokovic, B. V. Establishment and dysfunction of the blood-brain barrier. *Cell* **2015**, *163*, 1064–1078.
2 Ding, S. C.; Khan, A. I.; Cai, X. L.; Song, Y.; Lyu, Z. Y.; Du, D.; Dutta, P.; Lin, Y. H. Overcoming blood-brain barrier transport: advances in nanoparticle-based drug delivery strategies. *Mater. Today* **2020**, *37*, 112–125.
3 Teleanu, R. I.; Preda, M. D.; Niculescu, A. G.; Vladâcenco, O.; Radu, C. I.; Grumezescu, A. M.; Teleanu, D. M. Current strategies to enhance delivery of drugs across the blood-brain barrier. *Pharmaceutics* **2022**, *14*, 987.
4 Xie, J. B.; Shen, Z. Y.; Anraku, Y.; Kataoka, K.; Chen, X. Y. Nanomaterial-based blood-brain-barrier (BBB) crossing strategies. *Biomaterials* **2019**, *224*, 119491.
5 Wu, D.; Chen, Q.; Chen, X. J.; Han, F.; Chen, Z.; Wang, Y. The blood-brain barrier: structure, regulation, and drug delivery. *Signal Transduct. Target. Ther.* **2023**, *8*, 217.
6 Liebner, S.; Dijkhuizen, R. M.; Reiss, Y.; Plate, K. H.; Agalliu, D.; Constantin, G. Functional morphology of the blood-brain barrier in health and disease. *Acta Neuropathol.* **2018**, *135*, 311–336.
7 Zha, S.; Liu, H. T.; Li, H. D.; Li, H. L.; Wong, K. L.; All, A. H. Functionalized nanomaterials capable of crossing the blood-brain barrier. *ACS Nano* **2024**, *18*, 1820–1845.
8 Kim, W.; Kim, J.; Lee, S. Y.; Kim, H. M.; Jung, H. T.; Joo, K. M.; Nam, D. Functional validation of the simplified in vitro 3d co-culture based BBB model. *Biochem. Biophys. Res. Commun.* **2022**, *625*, 128–133.
9 Qiao, L.; Du, X. W.; Wang, H.; Wang, Z. Y.; Gao, S. J.; Zhao, C. Q. Research progress on the strategies for crossing the blood-brain barrier. *Mol. Pharm.* **2024**, *21*, 4786–4803.
10 Asimakidou, E.; Tan, J. K. S.; Zeng, J. L.; Lo, C. H. Blood-brain barrier-targeting nanoparticles: biomaterial properties and biomedical applications in translational neuroscience. *Pharmaceuticals* **2024**, *17*, 612.
11 Segarra, M.; Aburto, M. R.; Acker-Palmer, A. Blood-brain barrier dynamics to maintain brain homeostasis. *Trends Neurosci.* **2021**, *44*, 393–405.
12 Li, J.; Zheng, M.; Shimoni, O.; Banks, W. A.; Bush, A. I.; Gamble, J. R.; Shi, B. Y. Development of novel therapeutics targeting the blood-brain barrier: from barrier to carrier. *Adv. Sci.* **2021**, *8*, 2101090.
13 Alkhalifa, A. E.; Al-Ghraiybah, N. F.; Odum, J.; Shunnarah, J. G.; Austin, N.; Kaddoumi, A. Blood-brain barrier breakdown in alzheimer's disease: mechanisms and targeted strategies. *Int. J. Mol. Sci.* **2023**, *24*, 16288.
14 Pawar, B.; Vasdev, N.; Gupta, T.; Mhatre, M.; More, A.; Anup, N.;

Graphical Abstract

Boosting Blood-Brain Barrier Crossing with a Mannosylated Nanocarrier

Nan-Nan Gu, Ping Wei, Jin-Hui Jiang, and Jing-Hua Chen

Jiangnan University; Tongji University

A versatile mannosylated nanocarrier featuring blood-brain barrier (BBB) penetration and glioma cell targeting was designed. It enables the efficient delivery of a new aggregation-induced emission photosensitizer, thereby facilitating photodynamic therapy.

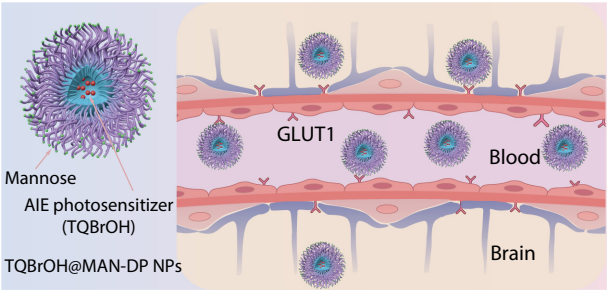

Chinese J. Polym. Sci. 2026, 44, 2524–2533 *https://doi.org/10.1007/s10118-026-3660-3*

Tekade, R. K. Current update on transcellular brain drug delivery. *Pharmaceutics* **2022**, *14*, 2719.
15 Tan, Q. X.; Zhao, S. J.; Xu, T.; Wang, Q.; Lan, M. H.; Yan, L.; Chen, X. F. Getting drugs to the brain: advances and prospects of organic nanoparticle delivery systems for assisting drugs to cross the blood-brain barrier. *J. Mat. Chem. B* **2022**, *10*, 9314–9333.
16 Lei, T.; Yang, Z. X.; Jiang, C. Q.; Wang, X. R.; Yang, W. Q.; Yang, X. T.; Xie, R.; Tong, F.; Xia, X.; Huang, Q. Q.; Du, Y. F.; Huang, Y.; Gao, H. L. Mannose-integrated nanoparticle hitchhike glucose transporter 1 recycling to overcome various barriers of oral delivery for alzheimer's disease therapy. *ACS Nano* **2024**, *18*, 3234–3250.
17 Du, D.; Chang, N. D.; Sun, S. L.; Li, M. H.; Yu, H.; Liu, M. F.; Liu, X. Y.; Wang, G. T.; Li, H. C.; Liu, X. P.; Geng, S. L.; Wang, Q.; Peng, H. S. The role of glucose transporters in the distribution of p-aminophenyl-α-D-mannopyranoside modified liposomes within mice brain. *J. Control. Release* **2014**, *182*, 99–110.
18 Yan, D. K.; Qu, X. W.; Chen, M. H.; Wang, J. H.; Li, X. Y.; Zhang, Z. X.; Liu, Y.; Kong, L.; Yu, Y.; Ju, R. J.; Li, X. T. Functionalized curcumin/ginsenoside Rb1 dual-loaded liposomes: targeting the blood-brain barrier and improving pathological features associated in APP/PS-1 mice. *J. Drug Deliv. Sci. Technol.* **2023**, *86*, 104633.
19 Jia, H. R.; Zheng, H.; Li, X.; Chen, X.; Liu, X. L.; Cao, Y. Y.; Zhang, S.; Zhang, J. N. D-mannose alleviates neurological deficits and inhibits NLRP3 inflammasome activation *via* the AMPK-mitophagy signaling pathway after traumatic brain injury. *Brain Res.* **2025**, *1869*, 150015.
20 Li, X. T.; Chen, L.; Huang, M. T.; Zeng, S. T.; Zheng, J. Y.; Peng, S. Y.; Wang, Y. Q.; Cheng, H.; Li, S. Y. Innovative strategies for photodynamic therapy against hypoxic tumor. *Asian J. Pharm. Sci.* **2023**, *18*, 100775.
21 Aebisher, D.; Rogóz, K.; Yakub, Z. A.; Dynarowicz, K.; Mysliwiec, A.; Mytych, W.; Komosinska-Vassev, K.; Misiolek, M.; Kawczyk-Krupka, A.; Bartusik-Aebisher, D. Photodynamic therapy in glioma cell culture. *Oncologie* **2024**, *26*, 885–897.
22 Correia, J. H.; Rodrigues, J. A.; Pimenta, S.; Dong, T.; Yang, Z. C. Photodynamic therapy review: principles, photosensitizers, applications, and future directions. *Pharmaceutics* **2021**, *13*, 1332.
23 Wu, D. D.; Chen, X. H.; Zhou, S. Q.; Li, B. Reactive oxidative species (ROS)-based nanomedicine for BBB crossing and glioma treatment: current status and future directions. *Front. Immunol.* **2023**, *14*, 1241791.
24 Kenry; Liu, B. Enhancing the theranostic performance of organic photosensitizers with aggregation-induced emission. *Acc. Mater. Res.* **2022**, *3*, 721–734.
25 Cheng, G. H.; Wang, H. J.; Zhang, C. N.; Hao, Y. F.; Wang, T. G.; Zhang, Y. Y.; Tian, Y.; Chang, J. Multifunctional nano-photosensitizer: a carrier-free aggregation-induced emission nanoparticle with efficient photosensitization and pH-responsibility. *Chem. Eng. J.* **2020**, *390*, 124447.
26 Yu, H.; Chen, B. J.; Huang, H. M.; He, Z. T.; Sun, J. M.; Wang, G.; Gu, X. G.; Tang, B. Z. AIE-active photosensitizers: manipulation of reactive oxygen species generation and applications in photodynamic therapy. *Biosensors-Basel* **2022**, *12*, 348.
27 Chen, Y. C.; Lam, J. W. Y.; Kwok, R. T. K.; Liu, B.; Tang, B. Z. Aggregation-induced emission: fundamental understanding and future developments. *Mater. Horiz.* **2019**, *6*, 428–433.
28 Cai, X. L.; Liu, B. Aggregation-induced emission: recent advances in materials and biomedical applications. *Angew. Chem. Int. Ed.* **2020**, *59*, 9868–9886.
29 Cho, C. F.; Wolfe, J.; Fadzen, C.; Calligaris, D.; Hornburg, K.; Chiocca, E. A.; Agar, N.; Pentelute, B.; Lawler, S. Blood-brain-barrier spheroids as an in vitro screening platform for brain-penetrating agents. *Neuro-Oncology* **2017**, *19*, 265–265.
30 Pérez-López, A.; Torres-Suárez, A. I.; Martín-Sabroso, C.; Aparicio-Blanco, J. An overview of in vitro 3d models of the blood-brain barrier as a tool to predict the in vivo permeability of nanomedicines. *Adv. Drug Deliv. Rev.* **2023**, *196*, 114816.
31 Qi, J. P.; Hu, X. W.; Dong, X. C.; Lu, Y.; Lu, H. P.; Zhao, W. L.; Wu, W. Towards more accurate bioimaging of drug nanocarriers: turning aggregation-caused quenching into a useful tool. *Adv. Drug Deliv. Rev.* **2019**, *143*, 206–225.
32 Kommidi, S. S. R.; Atkinson, K. M.; Smith, B. D. Steric protection of near-infrared fluorescent dyes for enhanced bioimaging. *J. Mat. Chem. B* **2024**, *12*, 8310–8320.
33 Kuronuma, Y.; Watanabe, R.; Hiruta, Y. The latest developments of near-infrared fluorescent probes from NIR-I to NIR-II for bioimaging. *Anal. Sci.* **2025**, *41*, 737–757.
34 Cheng, Y. H.; Cheng, H.; Jiang, C. X.; Qiu, X. F.; Wang, K. K.; Huan, W.; Yuan, A.; Wu, J. H.; Hu, Y. Q. Perfluorocarbon nanoparticles enhance reactive oxygen levels and tumour growth inhibition in photodynamic therapy. *Nat. Commun.* **2015**, *6*, 8785.
35 Wang, D. D.; Wu, H. H.; Phua, S. Z. F.; Yang, G. B.; Lim, W. Q.; Gu, L.; Qian, C.; Wang, H. B.; Guo, Z.; Chen, H. Z.; Zhao, Y. L. Self-assembled single-atom nanozyme for enhanced photodynamic therapy treatment of tumor. *Nat. Commun.* **2020**, *11*, 357.
36 Zhao, M. L.; Li, D. J.; Yuan, L.; Yue, Y. C.; Liu, H.; Sun, X. Differences in cytocompatibility and hemocompatibility between carbon nanotubes and nitrogen-doped carbon nanotubes. *Carbon* **2011**, *49*, 3125–3133.
37 Muniswamy, V. J.; Raval, N.; Gondaliya, P.; Tambe, V.; Kalia, K.; Tekade, R. K. 'Dendrimer-cationized-albumin' encrusted polymeric nanoparticle improves BBB penetration and anticancer activity of doxorubicin. *Int. J. Pharm*. **2019**, *555*, 77–99.
38 Yang, N.; Cao, C. Y.; Xu, C. S.; Su, Y.; Wang, W. J.; Song, X. J.; Liang, C.; Dong, X. C.; Mou, X. Z. Hypoxia-responsive nanoparticles for tumor-specific starvation therapy *via* a two-pronged approach. *Chem. Eng. J.* **2024**, *485*, 150133.
39 Zhang, R. S.; Li, Z. K.; Liu, J.; Deng, Y. T.; Jiang, Y. WZB117 enhanced the anti-tumor effect of apatinib against melanoma *via* blocking STAT3/PKM2 axis. *Front. Pharmacol.* **2022**, *13*, 976117.
40 Zheng, K.; Ouyang, X. M.; Li, J.; Cao, Y. B.; Peng, S. J. Zwitterionic sulfadiazine-based micelle achieves effective drug delivery to glioblastoma by overcoming multiple biological barriers. *J. Am. Chem. Soc.* **2025**, *147*, 34742–34757.
41 Yasinjan, F.; Xing, Y.; Geng, H. Y.; Guo, R.; Yang, L.; Liu, Z. L.; Wang, H. Immunotherapy: a promising approach for glioma treatment. *Front. Immunol.* **2023**, *14*, 1255611.
42 Zhang, C. B.; Cheng, W.; Ren, X. F.; Wang, Z.; Liu, X.; Li, G. Z.; Han, S.; Jiang, T.; Wu, A. H. Tumor purity as an underlying key factor in glioma. *Clin. Cancer Res.* **2017**, *23*, 6279–6291.

https://doi.org/10.1007/s10118-026-3660-3